Sensors and Materials, Vol. 37, No. 6 (2025) 2547–2568
MYU Tokyo

S & M 4074

Quantitative Evaluation of Point Cloud Deformations on Glass Surfaces Caused by Unmanned Aerial Vehicle Light Detection and Ranging Incidence Angle

Dohoon Kim,[1†] Kirim Lee,[2†] Kourosh Khoshelham,[3]
Hyeongil Shin,[1] and Won Hee Lee[4*]

[1]Department of Convergence and Fusion System Engineering, Kyungpook National University, Sangju 37224, Korea
[2]Research Institute of Artificial Intelligent Diagnosis Technology for Multi-Scale Organic and Inorganic Structure, Kyungpook National University, Sangju 37224, Korea
[3]Department of Infrastructure Engineering, University of Melbourne, Melbourne 3010, Australia
[4]Department of Location-Based Information System, Kyungpook National University, Sangju 37224, Korea

(Received September 6, 2024; accepted April 23, 2025)

Keywords: UAV, drone, LiDAR, point cloud, glass, glass deformation, incidence angle

Unmanned aerial vehicle (UAV) Light Detection and Ranging (LiDAR) is highly effective for the precise three-dimensional data collection of urban infrastructure and buildings, making it applicable in a variety of environments. However, the deformation—caused by the high transmittance and reflectance of glass, which vary with the LiDAR incidence angle—limits the accuracy and usability of the point cloud. In this study, we quantitatively evaluated the geometric deformation and intensity variation of glass surfaces with respect to the incidence angle of UAV LiDAR. For this research, point clouds of glass surfaces and control wall surfaces were collected at 10° incidence angle intervals from 0° to 70°, with the laser pulses being approximately perpendicular to the glass surface at 0°. Subsequently, the deformation of the glass surfaces was evaluated on the basis of calculated measurement errors and the extracted intensity for each incidence angle. The evaluation results revealed that changes in the incidence angle of UAV LiDAR affect the geometric deformation and intensity of the glass surface point clouds. Notably, the geometric deformation of the point clouds was minimized when the laser pulses were almost perpendicular to the glass surface, although the intensity spectrum broadened. Additionally, as the incidence angle increased, geometric deformation intensified, and the intensity approached zero. On the basis of these phenomena, we propose guidelines for setting the incidence angle of LiDAR to suit scanning purposes.

1. Introduction

Developments in geospatial engineering have introduced marked changes to various industries by enhancing operational efficiency and supporting decision-making through remote sensing. This evolution has underscored the necessity of collecting information on the 3D spatial

*Corresponding author: e-mail: wlee33@knu.ac.kr
†These authors contributed equally to this work.
https://doi.org/10.18494/SAM5362

ISSN 0914-4935

structure of the land cover. However, owing to the complexity of urban infrastructure, marked by the coexistence of various types of building, detailed 3D data collection using aerial photogrammetry and satellite remote sensing has been challenging. Recently, unmanned aerial vehicles (UAVs) have been used to address these challenges. UAVs offer high accessibility and precision for collecting 3D data in localized areas, making them the primary technology for gathering 3D data on building exteriors. Notably, photogrammetry using optical sensors and Light Detection and Ranging (LiDAR) sensors is employed in UAVs for 3D data collection.(1) LiDAR sensors produce a point cloud, which is a collection of 3D coordinate data, by calculating the time it takes for laser pulses to reflect off the surface of a real-world object and return to the sensor.(2) Owing to the inherent characteristics of LiDAR, which relies on laser pulse reflection from objects, the accuracy of data collection depends on the properties of the object, specifically its transmittance and reflectance.(3) Regarding vegetation, where penetration and reflection occur simultaneously, multiple returns from a single laser pulse provide rich information about the vegetation, including data from beneath the vegetation cover.(4) Conversely, objects with high transmittance and reflectance, such as glass surfaces or water, have markedly lower data collection accuracies, leading to various challenges.

For glass surfaces, despite the common perception that laser pulses generally pass through without scattering, deformation and holes occur when data is acquired using laser pulses with wavelengths such as 905 and 1550 nm, which are typically used for LiDAR. As a result, the point clouds and 3D models of building exteriors become distorted (e.g., Fig. 1). This glass surface deformation also occurs when 3D data is collected using LiDAR sensors mounted on UAVs, leading to the following problems with UAV LiDAR.

1) UAV LiDAR is well-suited for collecting data on buildings and land cover in localized areas, as it can access high-rise glass surfaces and building exteriors that are challenging for terrestrial LiDAR.(5) However, the reduction in data accuracy on glass surfaces impedes 3D modeling and studies utilizing point clouds, thereby compromising the usability of UAV LiDAR.(6) The reliance on UAV LiDAR for detailed 3D data collection, especially on building exteriors, highlights its vulnerability to glass surface deformations, which are less pronounced in high-altitude airborne LiDAR systems.
2) Studies on glass surface deformation have been extensively conducted using LiDAR data collected from terrestrial LiDAR or mobile terrestrial LiDAR.(7–10) Additionally, similar studies have been conducted in UAV photogrammetry, where glass surface deformation also occurs.(11–14) However, despite the critical impact of the glass surface on the quality of data, relevant research remains scarce.
3) The incidence angle of UAV LiDAR is more sensitive for glass surfaces than for other objects or LiDAR data collection methods, leading to various glass surface deformations. Consequently, these glass surface deformations due to the incidence angle hinder the establishment of UAV flight plans.(15,16)

These issues highlight the necessity for a thorough analysis of glass surface deformation based on UAV LiDAR incidence angles. Therefore, in this study, we quantitatively evaluated the geometric deformation and intensity of glass surfaces based on various UAV LiDAR incidence angles. Additionally, on the basis of the results of this quantitative evaluation, we summarized

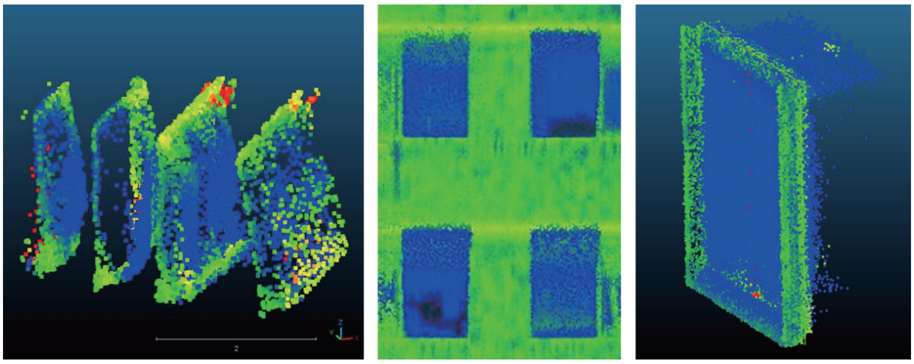

(a) (b) (c)

Fig. 1. (Color online) (a) Deformation, (b) holes, and (c) intensity reduction (e.g., blue points) observed on glass surfaces captured using UAV LiDAR.

the deformations that occur on glass surfaces at various incidence angles. In conclusion, we analyzed the impact of incidence angles on glass surface deformation and proposed methods for setting appropriate incidence angles when planning UAV flights.

2. Materials and Methods

We performed the following steps, as shown in the research flowchart in Fig. 2: point cloud collection, data preprocessing, and analysis. We collected point clouds at incidence angles ranging from −5° to 74°, taking the alignment where the laser pulses are perpendicular to the glass surface (i.e., at 0°) as the baseline. We then performed data preprocessing and manual data extraction of the study targets from the collected data. In addition, a virtual plane was generated to calculate measurement errors. Using the extracted study data and the virtual plane, we calculated the measurement errors for each point in the data. Finally, we analyzed the measurement errors and intensity according to the angles, summarizing the glass surface deformations.

2.1 Study area and targets

For the study area, we selected the flat façade of Building No. 9, located at 2559 Gyeongsang-daero, Sangju-si, Gyeongsangbuk-do, Republic of Korea, which features numerous windows of uniform size and composition. The façade primarily consists of orange brick wall surfaces, making it suitable for comparative evaluation. We selected windows within the study area free of obstacles that could hinder accuracy. The selected windows are single-pane windows of 1 cm thickness. To minimize the impact of contamination and the properties of applied insulation materials, we selected windows of the same model installed at the same time. For the control group used in the comparative evaluation, we selected wall surfaces within the study area made of typical bricks and concrete, with no surrounding obstacles.

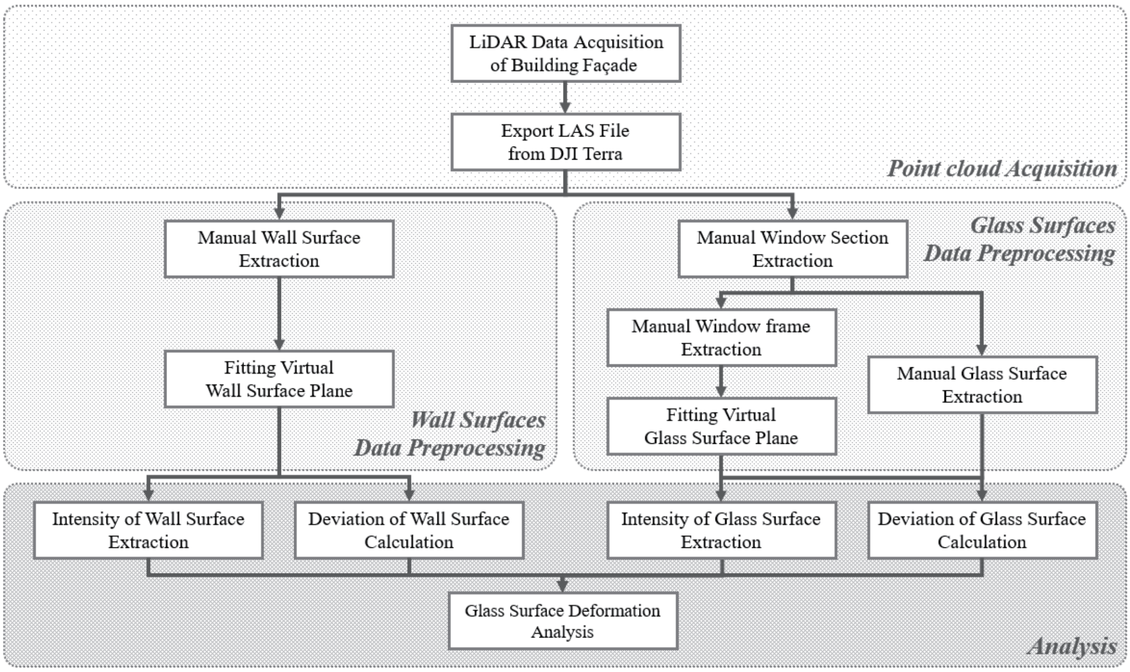

Fig. 2. Research flowchart showing the steps involved in this study.

2.2 Research equipment

In this study, we used three pieces of research equipment, as listed in Table 1. We used the Real-Time Kinematic Global Navigation Satellite System (RTK-GNSS) based on DJI's D-RTK2 to ensure positional accuracy during the flights.(17) The DJI L1 LiDAR sensor was used for data collection, which incorporates the Livox Avia sensor operating in the 905 nm band. Owing to the variation in reflection and transmission patterns across different LiDAR bands, we selected the widely used 905-nm-band LiDAR sensor for this study. The DJI L1 sensor can collect data using repetitive and nonrepetitive scan patterns (e.g., Fig. 3).(18) Because we focused on the incidence angle between the glass surface and the sensor, we adopted the nonrepetitive scan pattern, which has a wide vertical Field of View (FOV) (77.2°) and higher point density toward the center.

2.3 Data collection

To analyze the deformation based on incidence angles, we adjusted the aim of the sensor in increments of 10°, covering an incidence angle range from −5° to 74°. Eight flights were performed for each of the following angle ranges: −5° to 4°, 5° to 14°, 15° to 24°, 25° to 34°, 35° to 44°, 45° to 54°, 55° to 64°, and 65° to 74° [Fig. 4(a)]. All flights were conducted under controlled conditions as listed in Table 2, with a consistent path of the sensor's aim illustrated in Fig. 5; only the sensor's incidence angle range varied. The parameters included a distance of 10 m between the glass surface and the sensor, a flight speed of 0.5 m/s, identical LiDAR sensor settings, and the same path of sensor's aim [Fig. 4(b)]. The distance between the glass surface

Table 1
(Color online) Specifications of research equipment used in this study.

 DJI Zenmuse L1	Laser Wavelength	905 nm
	System Accuracy	Horizontal: 10 cm @ 50 m (RMS) Vertical: 5 cm @ 50 m (RMS)
	Maximum Returns Supported	3
	FOV	Nonrepetitive: 70.4° × 77.2° Repetitive: 70.4° × 4.5°
 DJI D-RTK2 Station	GNSS Frequency	GPS: L1, L2, L5 BeiDou: B1, B2, B3 GLONASS: F1, F2 Galileo: E1, E5A, E5B
	RTK Positioning Accuracy	Horizontal: 1 cm + 1 ppm (RMS) Vertical: 2 cm + 1 ppm (RMS)
 DJI Matrice 300 RTK	Hovering Accuracy (Windless or breezy)	Vertical ±0.5 m (P-mode with GPS) ±0.1 m (D-RTK) Horizontal ±1.5 m (P-mode with GPS) ±0.1 m (D-RTK)

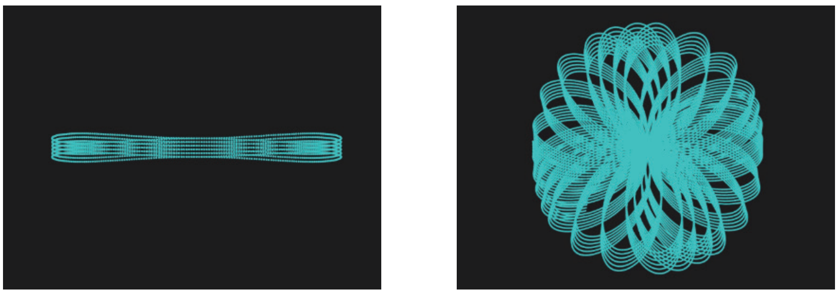

(a) (b)

Fig. 3. (Color online) (a) Repetitive and (b) nonrepetitive scan patterns of DJI L1.

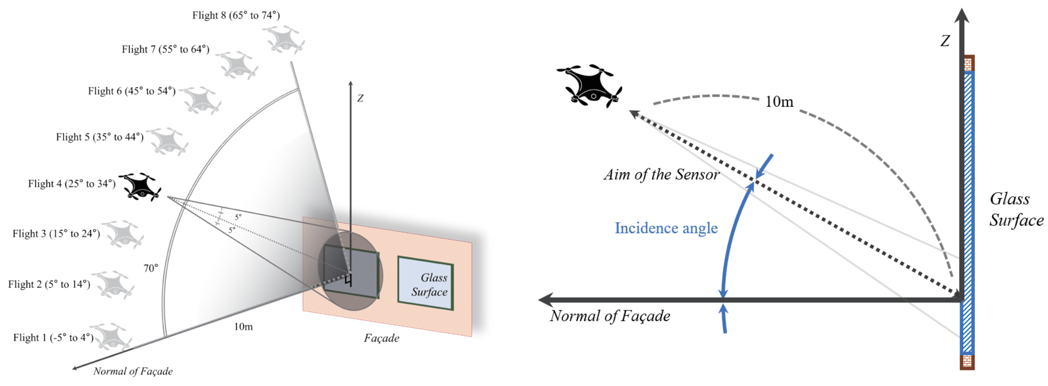

(a) (b)

Fig. 4. (Color online) Schematics of flight and scanning methods for data collection.

Table 2
Variable settings for each flight in data collection.

Flight	Flight 1	Flight 2	Flight 3	Flight 4	Flight 5	Flight 6	Flight 7	Flight 8
Aim of the Sensor (Incidence Angle Range)	0° (Horizontal) (−5° to 4°)	10° (5° to 14°)	20° (15° to 24°)	30° (25° to 34°)	40° (35° to 44°)	50° (45° to 54°)	60° (55° to 64°)	70° (65° to 74°)
Study Area	BLDG. No. 9, 2559, Gyeongsang-daero, Sangju-si, Gyeongsangbuk-do, Republic of Korea							
Target	Wall Surfaces, Glass Surfaces							
Distance	10 m							
Flight Speed	0.5 m/s							
LiDAR Setting	Nonrepetitive Scan Pattern, Multiple Return (3), 160 Hz							

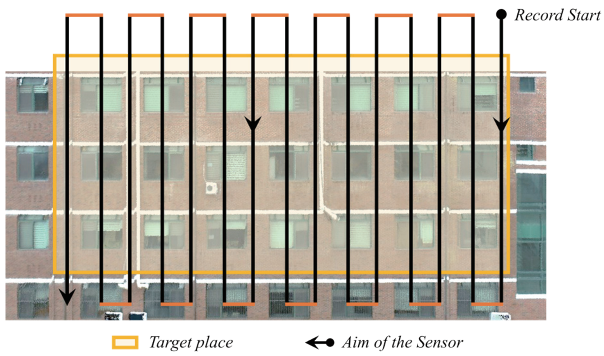

Fig. 5. (Color online) Target area for data collection and path of the sensor's aim during acquisition.

and the sensor, flight speed, and flight path can affect the point density of the data.(19) Thus, these parameters were consistently controlled across all flights. Each flight lasted 10 min, and according to the DJI L1 user manual, IMU calibration was performed every 100 s during data collection to prevent accuracy degradation, as per the DJI L1 user manual. Because multiple reflections often occur on glass surfaces, we used the triple reflection setting, the maximum supported by the DJI L1. The nonrepetitive scan pattern used for data collection had a FOV of 70.4° × 77.2°, which can interfere with the study by capturing a wide range of incidence angles between the glass surface and the sensor. Therefore, to ensure that data excessively deviating from the aim of the sensor did not interfere with the study, we extracted point clouds within a 5° × 5° range centered on the aim of the sensor, corresponding to the incidence angle ranges determined by the aim of the sensor in increments of 10° for the analysis. The collected data was reconstructed using DJI Terra and then exported in LAS format, the standard data format for point cloud data.

2.4 Data filtering

We extracted the LAS files using CloudCompare to remove unnecessary information, namely, that outside the study area. We then exported the study area as a PTS file format, which is an ASCII format for point cloud data. These files list the information for each point in rows and the indices in columns, making the data easy to process. From the extracted study area data, we filtered out unnecessary indices and points with incidence angles outside the range from −5° to 4°. This was to ensure that incidence angles within the 5° × 5° range for each flight were utilized as previously explained. Additionally, owing to the characteristics of the DJI L1 sensor, where angles are recorded as integers, filtering the range from −5° to 4° allowed the data to align with the 10° increments of the aim of the sensor after rounding. Using Python, we filtered out 65% of unnecessary data, resulting in a refined PTS file format for the study area.

2.5 Data extraction

We extracted both glass surfaces and wall surfaces from the data collected at various incidence angles. All target extraction tasks were performed manually using the cross section tool in the CloudCompare software.

Owing to the deformation of the glass surfaces in the collected point clouds, determining the exact position of the actual glass surface is challenging. Therefore, we assumed the window frame, which has relatively low transmittance and reflectance and thus higher data collection accuracy, as the actual position of the glass surface.[20] This assumption served as the basis for calculating the measurement error and root mean square error (*RMSE*) for the glass surfaces. Extraction was performed in two steps: the entire window including the frame was first manually extracted, followed by the manual extraction of the glass surface.

For this study, we extracted all glass surfaces and wall surfaces, excluding window frames, to the same dimensions of 1.05 × 1.00 × 1.40 m^3, as shown in Fig. 6. This extraction was performed on the basis of the size of the target windows and by ensuring that no other objects aside from the glass or wall surfaces were included.

2.6 Virtual plane generation

Point clouds are composed of points with coordinates, making it difficult to select a single reference value. Therefore, in this study, we created virtual planes representing the assumed true positions of the wall and glass surfaces. These virtual planes were used as the basis for the

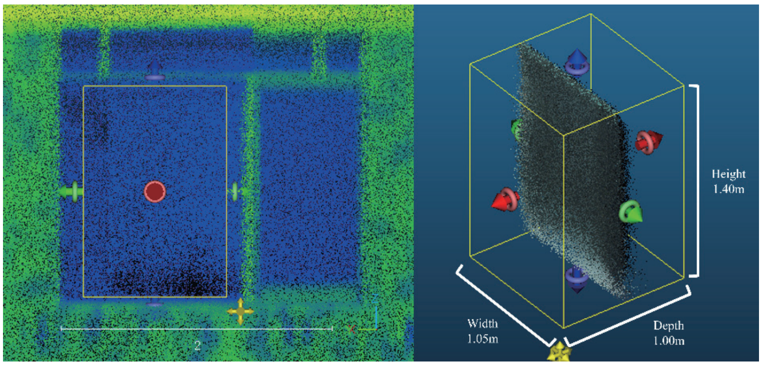

(a) (b)

Fig. 6. (Color online) (a) Example of glass and wall surface extraction and (b) extraction criteria.

quantitative evaluation by calculating the deviations between the points and the planes. For the glass surfaces, we generated virtual planes on the basis of previously extracted window frames (e.g., Fig. 7). For the wall surfaces, we used the fit plane tool to generate virtual planes, which generates a plane using standard least square fitting based on the eigenvalues and vectors of the covariance matrix. This tool is well-suited for creating a reference plane of the flat wall surface from a scattered point cloud. These processes were performed using the create plane and fit plane tools in CloudCompare software. Subsequently, we extracted the plane data in an ASCII file format consisting of the central point of the virtual plane and the coefficients of the equation of the plane for use in error calculations.

2.7 Measurement error calculation

The measurement error was calculated for all points using the virtual glass plane and the virtual wall plane as references. This measurement error represents the perpendicular distance between each point in the collected point cloud and the generated virtual plane, indicating how far the point cloud data deviates from the actual glass and wall surfaces. Equation (1) was used for the calculations. For the plane data, coefficients A, B, and C from the equation of plane for x, y, and z, respectively, were utilized in Eq. (1). Because the D coefficient was not included in the extracted ASCII file of the plane, it was calculated using the coordinates of the plane's central point, which were provided in the file, and then applied in Eq. (1). Coordinates x_p, y_p, and z_p of the collected points were used in the equation.

$$Measurement\ Error = \frac{Ax_p + By_p + Cz_p + D}{\sqrt{A^2 + B^2 + C^2}} \tag{1}$$

We calculated the measurement error for all extracted glass and wall surfaces by computing Eq. (1). Python was used to create the results, which included the extraction of each point's height (z), incidence angle, and intensity for the quantitative evaluation of measurement error.

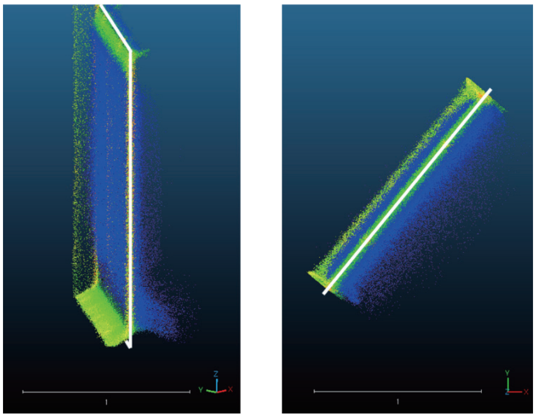

Fig. 7. (Color online) Example of virtual glass plane generation based on the window frame.

3. Results

The quantitative evaluation for analyzing glass surface deformation was conducted on the basis of point distribution by height, measurement error, and intensity. Using data collected across eight incidence angles ranging from −5° to 74°, centered around 0° acquisition where the glass surface and laser pulses are perpendicular, we calculated the quartiles of points by height, the quartiles of measurement error, the mean of measurement error, *RMSE*, standard deviation, quartiles of intensity, and intensities over 100 for analysis.

3.1 Point distribution by height

For the quantitative evaluation of point distribution by height, we calculated the quartiles of points by height. From the 1.4 m height data extracted from the glass and wall surfaces, points closer to 0 m represent the lower part of the objects, whereas points closer to 1.4 m represent the upper part of the objects.

Figure 8 shows the interquartile range (IQR) and median of points by height. This graph shows the concentration of points by heights from the bottom to the top of the glass and wall surfaces, which demonstrates how the points on the lower part of the glass surface were not properly captured as the incidence angle increased. The point distribution by height for each object at 0° acquisition exhibits almost identical IQR and median values for both the glass and wall surfaces. The points for both objects maintained an IQR and median within an error range of ±0.05 m up to the 10° acquisition. However, starting from the 20° acquisition, as the incidence angle increased, the quartiles of points by height for the glass surface rise, and the IQR decreased. At the 70° acquisition, the median of the glass surface points by height peaked at 1.1738 m. This value indicates that the median of glass surface points by height is located at 84% of the maximum height of 1.4 m.

Figure 9 shows the density plot of points by height collected at each incidence angle. This density plot also allows for the identification of heights where points are concentrated or lacking

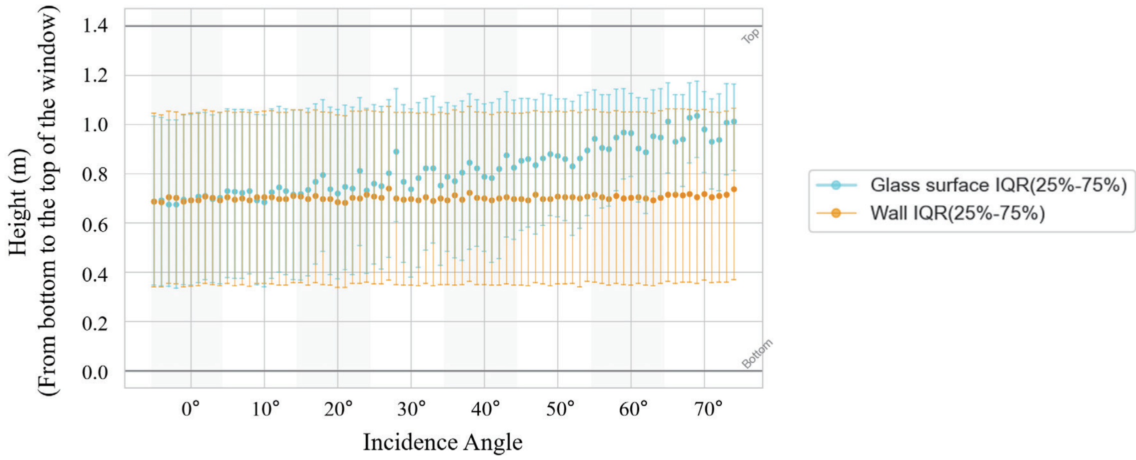

Fig. 8. (Color online) Quartiles, IQR, and median of points by height for glass surfaces and wall.

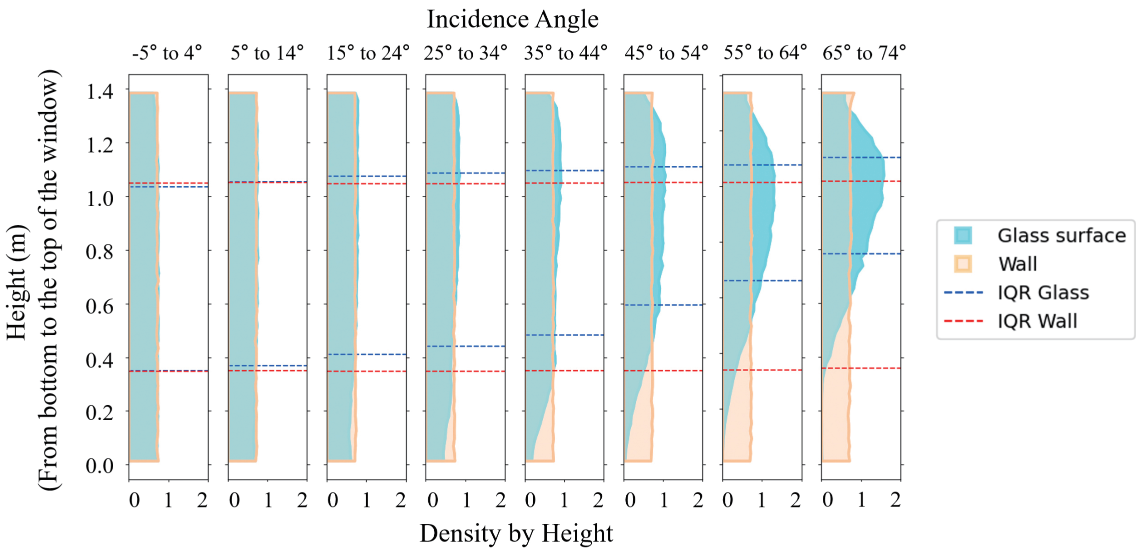

Fig. 9. (Color online) Density plot of points by height for glass surfaces and wall.

to observe point loss in the lower part of the glass surface. At 0° and 10° acquisitions, the data for the glass and wall surfaces exhibited almost identical densities at all heights, with similar quartiles. Starting from the 20° acquisition, as observed in Fig. 9, as the incidence angle increases, the quartiles of the glass surface increase, and a reduction in density is observed in the lower part of the glass surface. This trend continued up to the maximum incidence angle of 70°, with the quartiles of the glass surface increasing and density concentrating toward the upper part. In contrast, the wall surface, which served as the control group, maintained nearly identical interquartile ranges and point densities across all incidence angles.

3.2 Measurement error

We calculated the quartiles of measurement error, mean measurement error, *RMSE*, and the standard deviation of points at different incidence angles for the perpendicular direction of the glass surface. These metrics are suitable for evaluating how well the collected point cloud represents the actual glass and wall surfaces or how dispersed the points are in comparison. Measurement error is represented as positive for points behind the virtual object plane and negative for points in front, on the basis of the data acquisition direction of the sensor. For the wall surface, *RMSE* was excluded, as the *RMSE* and standard deviation are identical owing to the process of creating the virtual wall plane using *RMS*.

The glass surface shows the lowest average *RMSE* of 0.02693 m at 0° acquisition (Fig. 10). However, *RMSE* continues to increase until 40° acquisition and then decreases. The lowest *RMSE* values were observed between −1° and 1° (0.022102, 0.021356, and 0.024953 m), and *RMSE* values above 0.025 m were found at all other incidence angles. The highest average *RMSE* of 0.04343 m was recorded at 40° acquisition. Beyond this acquisition, as the incidence angle increased, the *RMSE* decreased again.

Figure 11 shows the measurement error distribution by height from the bottom to the top of the glass surface, along with the median calculated in 0.1 m increments. At 0° acquisition, the

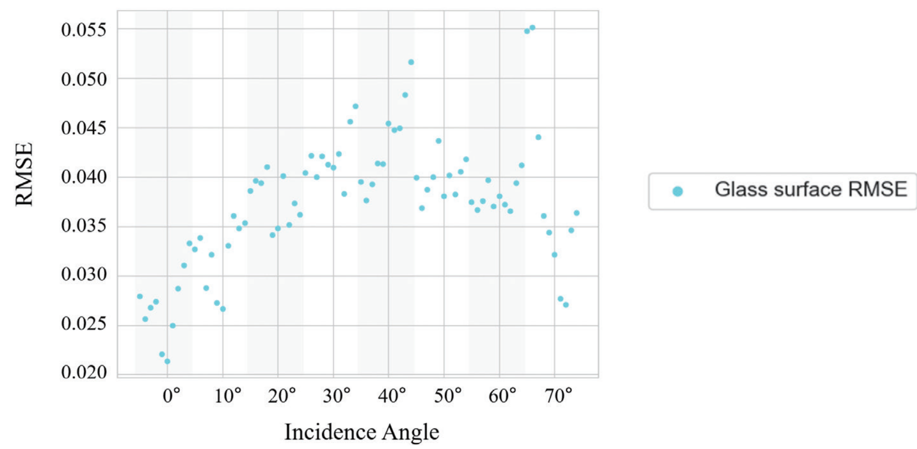

Fig. 10. (Color online) Scatter plot of RMSE for glass surface by incidence angle.

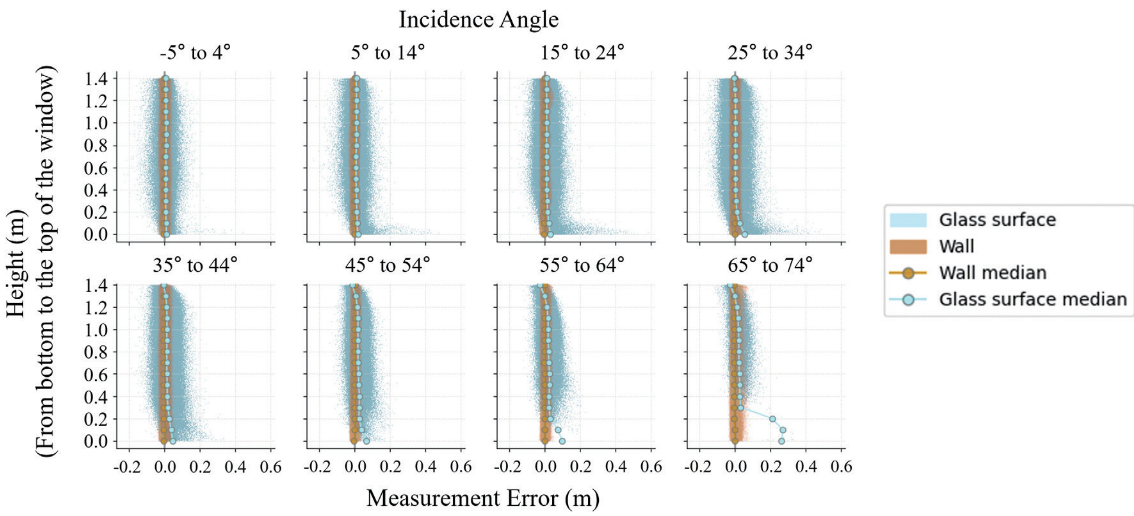

Fig. 11. (Color online) Scatter plot of measurement error distribution by height and incidence angle.

distribution of points on the glass surface was most similar to that on the wall surface. However, starting from the 10° acquisition, the positive measurement error was concentrated behind the glass surface. In contrast to the wall surface, which shows a uniform distribution of measurement error across all incidence angles, the glass surface exhibited a different pattern: negative measurement errors predominantly occurred at the upper part, whereas positive measurement errors were concentrated in the middle and lower parts. Additionally, as the incidence angle increases, a point loss occurs at the lower part of the glass surface.

Figure 12 shows that the measurement error for the glass surface is predominantly positive. The median measurement error for the glass surface is positive across all incidence angles and exhibits a much broader spectrum of measurement errors than the wall surface. For the wall surface, all points fell within the measurement error range from −0.06 to 0.11 m for all incidence angles except at 70° acquisition. However, the glass surface deviated significantly from this range at all incidence angles, displaying noticeable noise. The glass surface exhibited greater dispersion than the control wall surface, resulting in a relatively wide distribution, as depicted in Fig. 13.

Figure 13 shows that the standard deviation of measurement error for the glass surface is generally larger than that for the wall surface, indicating a broader distribution. The distribution of the glass surface is most concentrated at 0° acquisition, with an average standard deviation of 0.02502 m. However, this value is still significantly higher than the average standard deviation of 0.00997 m observed for the wall surface across all incidence angles. The same pattern as the *RMSE* was observed in the standard deviation of the glass surface, with higher average standard deviations recorded at 30° and 40° acquisitions (0.04066 and 0.04343 m, respectively), indicating a broader distribution. The wall surface maintained a low standard deviation, but it increased at 70° acquisition, indicating a decrease in data accuracy.

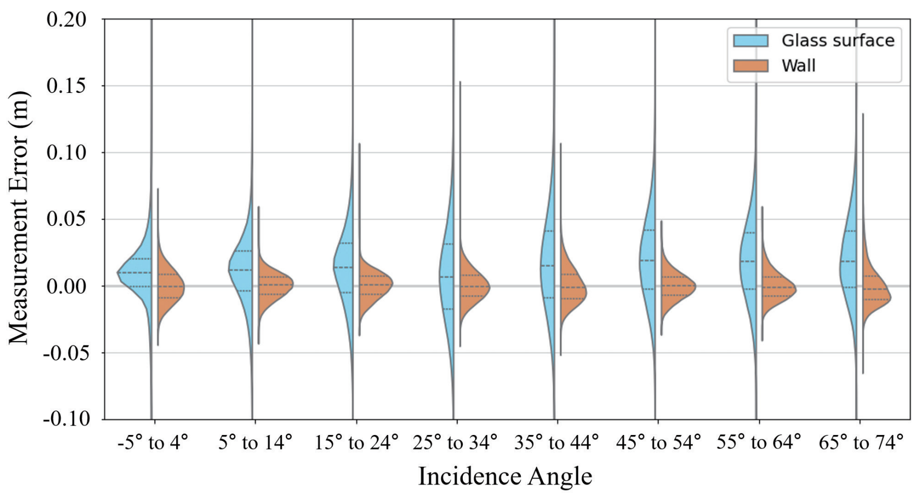

Fig. 12. (Color online) Violin plot of measurement error distribution by incidence angle.

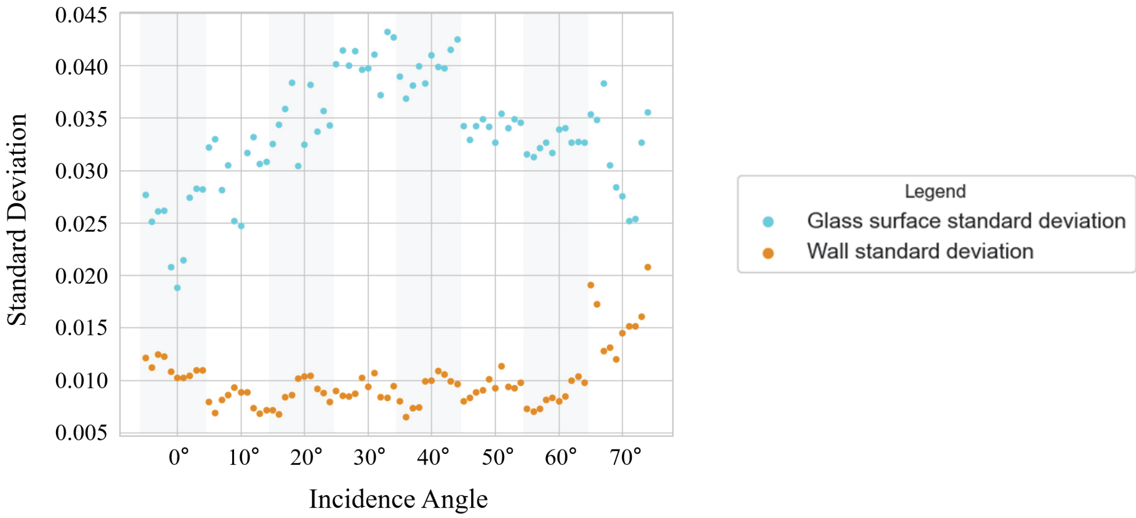

Fig. 13. (Color online) Scatter plot of standard deviation by incidence angle.

3.3 Intensity

For the intensity analysis, we calculated the intensity quartiles, intensity mean, and the number of points with an intensity greater than 100, for each incidence angle. These metrics are suitable for evaluating the variation in the intensity of the glass and wall surface points as the incidence angle changes.

The intensity of the glass surface was consistently lower than that of the wall surface across all incidence angles. The median intensity of the glass surface was zero at incidence angles ranging from 20° to 70°. Additionally, for incidence angles of 30° and above, the mean intensity of the glass surface was below 0.5, and over 75% of the points had an intensity of zero. Notably, the highest intensity for the glass surface was observed at 0° acquisition. Moreover, at 0°, 10°, and 20° acquisitions, the mean intensity of the glass surface was significantly higher than the median, which was attributed to some points exhibiting very high intensity. Whereas only four points had an intensity greater than 100 on the wall surface across all incidence angles, the glass surface had a total of 12,359 such points across all angles, with 4,134 of these points being collected at 0°, representing the highest concentration. Figure 14 shows a high occurrence of outliers in the glass surface at incidence angles close to 0° and 10°. Furthermore, Fig. 14 indicates that, on the glass surface, the density of points with intensity greater than 100 increases as the incidence angle approaches the aim of the sensor, suggesting that this phenomenon was concentrated around the aim of the sensor.

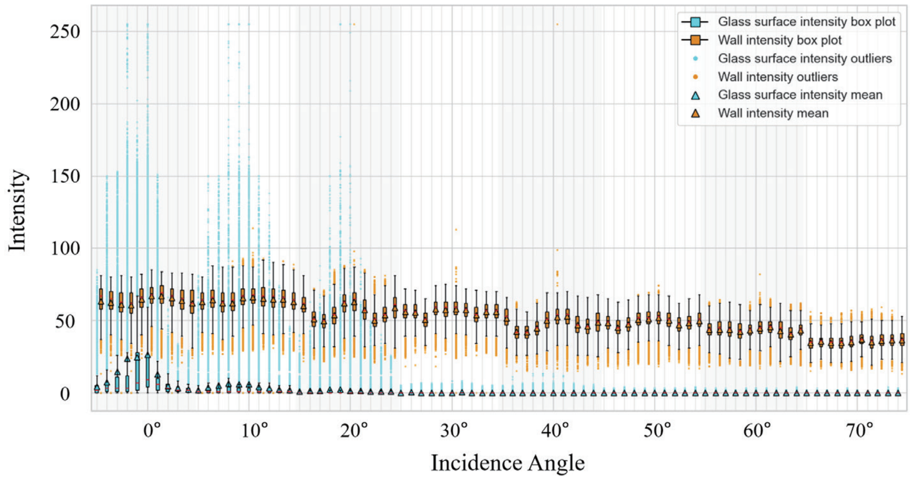

Fig. 14. (Color online) Box plot of intensity by incidence angle.

4. Discussion

4.1 Glass surface point loss

The results revealed that point loss on the glass surface begins to occur at an incidence angle of 20°. In the point cloud, glass surface point loss appears as gaps or holes, as shown in Fig. 15. This phenomenon is affected by the incidence angle and becomes more pronounced as the incidence angle increases. The most severe point loss was observed at the highest IQR by height during the 70° acquisition, the maximum incidence angle used in this study. Additionally, the IQR of points by height and the density of points by height for the glass surface at 0° acquisition were not significantly different from those of the control wall surface, indicating that point loss on the glass surface is minimal at 0° acquisition.

The point loss on the glass surface likely occurred because the reflected laser pulse intensity from the glass surface was either below the threshold or, despite exceeding the threshold, was not classified as a point during the waveform decomposition of the DJI L1 sensor. This phenomenon was particularly concentrated in the lower part of the glass surface. Presumably, laser pulses, which were either fully reflected or transmitted through the glass surface, were reflected off the window frame or sill, resulting in intensity peaks being recorded. During the decomposition of the sensor's waveform, the lower intensity from the glass surface was likely overshadowed by the intensity peaks from other objects, leading to it not being detected as a point on the glass surface (Fig. 16). This observation is further supported by the increased point loss occurring on the lower part of the glass surface near the window frame and sill as the incidence angle increases.

The point loss on glass surfaces causes challenges where gaps appear in 3D models, resulting in an inaccurate representation of the actual surface. The findings revealed that the point loss that leads to the appearance of holes in the 3D model of glass surfaces begins at an incidence angle of approximately 50°. For instance, UAV LiDAR, which collects data aerially, often

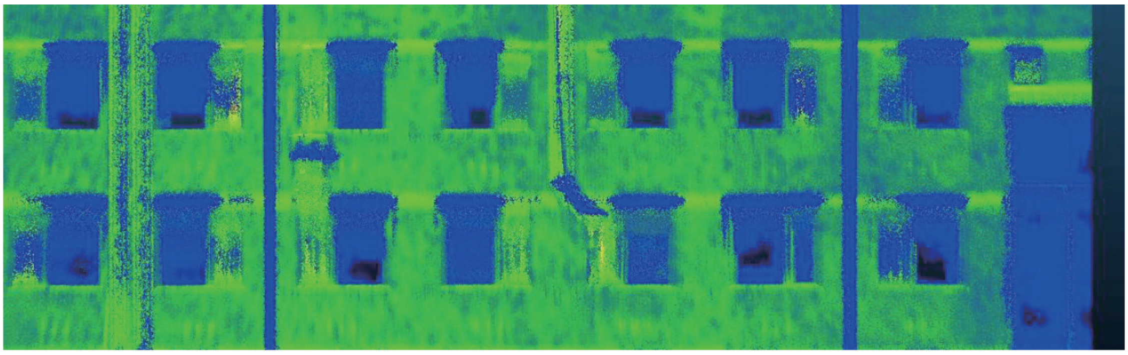

Fig. 15. (Color online) Glass surface point loss at 70° acquisition.

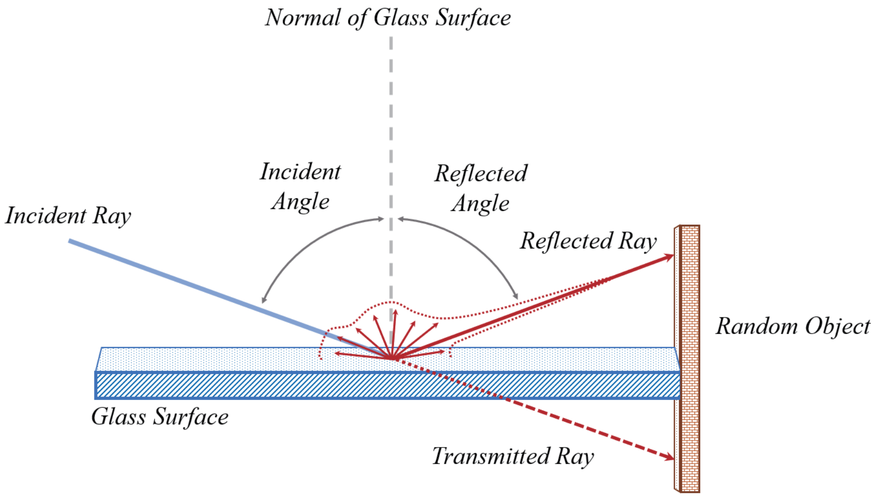

Fig. 16. (Color online) Causes of glass surface point loss.

struggles to capture data in areas such as building entrances or the lower sections of roofs owing to the structure of the building. However, the point loss on glass surfaces occurs regardless of structure, thereby further compromising the accuracy of the UAV LiDAR point cloud.

4.2 Glass surface distortion

The wall surface exhibited a standard deviation consistent with the L1 sensor specifications, except at the 70° acquisition. This aligns with a previous study, which showed a significant increase in noise at incidence angles above 70°.[10] However, glass surface distortion was characterized by higher *RMSE* and standard deviation than wall surface distortion. Across all incidence angles, the glass surface exhibited a much larger standard deviation, resulting in the wide distribution of glass surface points as shown in Fig. 17. Point cloud collected from the glass surface did not accurately represent its actual shape. The accuracy of the glass surface point cloud collected in the vertical direction was less than one-third of the accuracy observed on the wall surface under identical acquisition conditions. Additionally, the measurement error on the

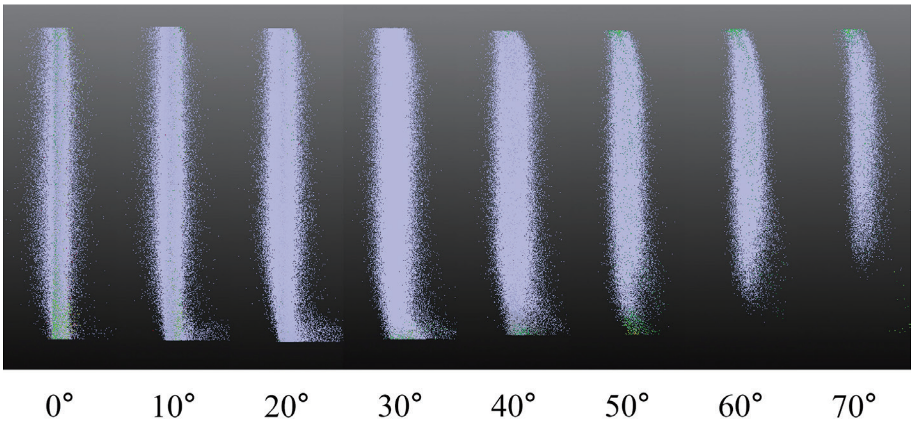

Fig. 17. (Color online) Right-side view of point clouds showing glass surface distortion according to the incidence angle.

glass surface exhibited two unusual patterns. First, the median measurement error for all incidence angles was positive, indicating that the majority of points were collected behind the assumed virtual glass plane and that the point cloud was generally shifted backward. Second, starting from the 10° acquisition, negative measurement errors were predominantly observed in the upper part of the glass surface, whereas positive measurement errors were more common in the middle and lower parts. This indicates that the glass surface, which is actually flat, was represented as a curved shape in the LiDAR point cloud.

Glass surface distortion was observed across all incidence angles, but it was minimal at 0° acquisition. At this angle, the glass surface did not exhibit a curved shape but maintained an even shape. However, as the incidence angle increased, both the standard deviation and *RMSE* for the glass surface also increased, with the most severe distortion occurring at 30° and 40° acquisition. From 50° acquisition onward, point loss became more pronounced, making it difficult to analyze glass surface distortion.

Glass surface distortion is likely caused by the reflective and transmissive properties of the glass surface as well as its thickness. Most objects typically have low transmittance, causing them to reflect a single laser pulse off their surface [Fig. 18(a)]. However, glass surfaces, with their high transmittance, allow laser pulses to penetrate, leading to potentially multiple reflections both on and within the glass [Fig. 18(b)]. This could explain the higher measurement error and standard deviation on glass surfaces. At incidence angles of 0° and 10°, more points were collected from the glass surface than from the wall surface, suggesting that multiple reflections occurred within the glass owing to its thickness, as shown in Fig. 18(b). Additionally, as the incidence angle increases, the effective thickness of the glass that the laser pulse traverses also increases. This provides further evidence for the trend shown in Fig. 12, where measurement error increases as the incidence angle increases.

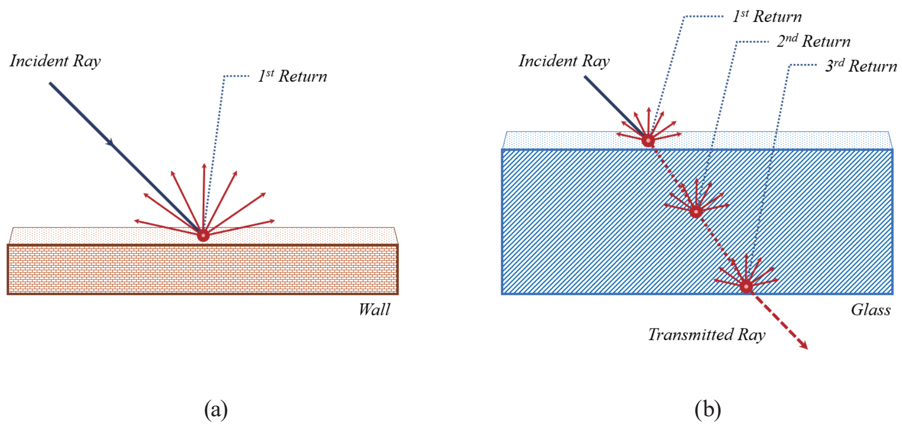

Fig. 18. (Color online) Causes of glass surface distortion on (a) wall and (b) glass.

4.3 Intensity peaking

Intensity peaking was observed on the glass surface, in which the intensity was significantly higher near the aim of the sensor. This phenomenon followed the direction of the sensor's movement according to the UAV's flight path. The density of points on the glass surface with an intensity greater than 100 increased as the sensor became more perpendicular to the glass surface and as the points were closer to the aim of the sensor. Therefore, intensity peaking was concentrated at the 0° acquisition.

Intensity peaking was observed exclusively on the glass surface. Figure 19 shows the points with intensity values ranging from 150 to 255 from the entire dataset at 0° acquisition. All points with an intensity exceeding 150 were found to be within the glass surface area, as indicated by the gray dashed line. Notably, the points with intensity values above 250, highlighted in red in Fig. 19, were only observed when the sensor was perpendicular to the glass surface.

The intensity peaking is attributed to the reflective properties of the glass surface. The wall surface exhibited a consistent intensity range for all points, primarily owing to diffuse reflection and the absence of laser pulse transmission through the surface, as shown in Fig. 20(a). In contrast, the glass surface, with its high transmittance and reflectance, exhibited a variety of reflection patterns. Koch *et al.* observed irregular intensity patterns on glass surfaces depending on the incidence angle and distance.[9] Similarly, we found that the intensity spectrum for the glass surface point cloud was notably broad. Specifically, as shown in Fig. 20(b), when the incident laser pulse was closer to the normal of the glass surface, the increase in specular reflection intensity reaching the sensor appears to have caused intensity peaking. This observation further supports the conclusion that intensity peaking was concentrated at the 0° acquisition.

This intensity peaking can affect the usability of LiDAR intensity data. In a previous study the occurrence of intensity peaking under certain conditions was utilized to detect glass surfaces.[8] This suggests that while intensity peaking is one of the distortions, it may also be leveraged for glass surface analysis in LiDAR point clouds.

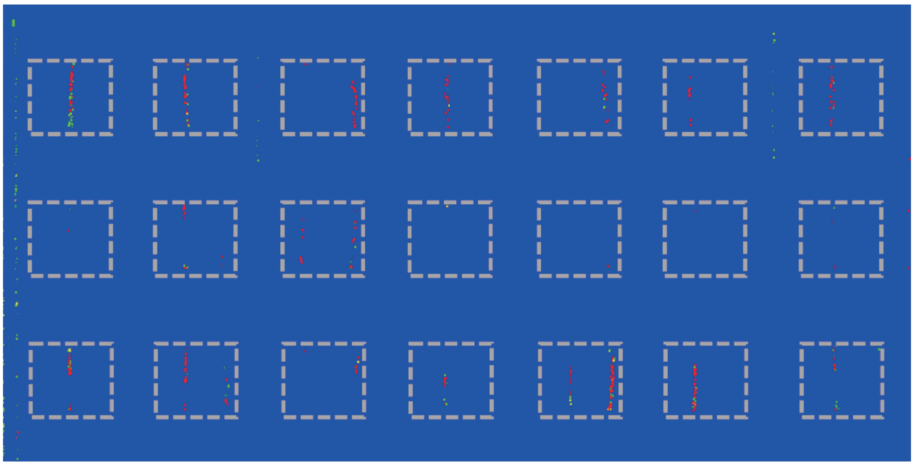

Fig. 19. (Color online) Points with intensities of 150–255 in the 0° acquisition dataset.

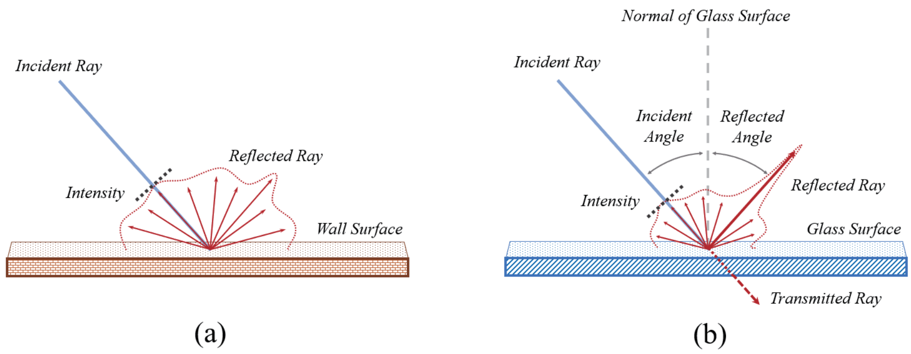

Fig. 20. (Color online) Causes of intensity peaking on (a) wall and (b) glass.

4.4 Intensity reduction

Lastly, apart from the points exhibiting intensity peaking, most of the points on the glass surface exhibited an intensity reduction, with intensity values falling below 5. This intensity reduction was consistently observed across all incidence angles. Thus, the intensity of the glass surface point cloud was clearly distinct, setting it apart from the wall surface where no significant reduction was observed, as shown in Fig. 21. Starting from the 20° incidence angle, more than half of the points on the glass surface had an intensity of 0 because of this phenomenon, and the intensity reduction became more pronounced as the incidence angle increased. This suggests that reflected laser pulses that barely exceeded the threshold during the waveform decomposition of the DJI L1 sensor were recorded as points.

The intensity reduction on the glass surface is likely caused by the same factors as those for the intensity peaking, primarily the high transmittance and reflectance of the glass surface [Fig. 20(b)]. The high transmittance of the glass surface means that it allows some laser pulses to pass through it, whereas the high reflectance causes specular reflection in most of the reflected

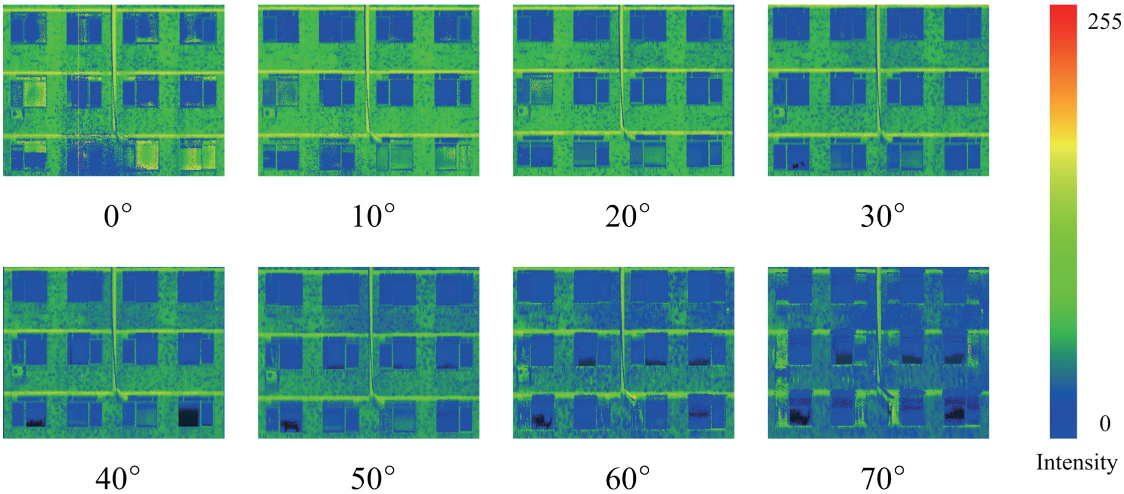

Fig. 21. (Color online) Glass surface intensity reduction across all incidence angles.

pulses, resulting in only a minimal amount of laser pulse reaching the LiDAR sensor. Additionally, as the incidence angle increases, it becomes more difficult for reflected laser pulses to reach the sensor, leading to a decrease in the degree of intensity peaking and an increase in the degree of intensity reduction across most of the points.

5. Conclusions

In this study, we confirmed that the following glass surface deformations occur in the point cloud acquired using UAV LiDAR, compared with the control wall surface: glass surface point loss, glass surface distortion, intensity peaking, and intensity reduction. These phenomena are unique to glass surface point clouds, primarily because of the high transmittance and reflectance of glass. Additionally, glass surface deformations were observed to interfere with the accurate acquisition of point cloud data using UAV LiDAR sensors. We also revealed that the severity of these deformations is closely linked to the UAV LiDAR incidence angle, emphasizing the need to carefully consider this factor when planning data collection. On the basis of the results of this study, the following incidence angle settings are recommended when planning UAV LiDAR flights to minimize glass surface deformations.

1) 0° incidence angle: This angle is recommended when it is crucial to minimize geometric deformation of the glass surface or when collecting building façade data through vertical flight paths. At 0° acquisition, no glass surface point loss was observed, and the lowest *RMSE* and standard deviation were recorded, indicating minimal geometric deformation of the glass surface and a more uniform shape.
2) 20°–40° incidence angle: For applications requiring uniform intensity across the glass surface, an incidence angle between 20° and 40° is recommended. Although the 0° and 10° incidence angles resulted in a wide intensity spectrum because of intensity peaking, the 20° incidence angle onwards exhibited low and uniform intensities, which was attributed to intensity reduction.

3) Avoidance of 50° incidence angle and above: It is generally not recommended to use an incidence angle of 50° or higher in most UAV LiDAR data collection scenarios, where both the upper parts of buildings and uniform glass surface data are required. Starting from a 50° incidence angle, glass surface point loss becomes considerable, leading to holes in the point cloud, and geometric distortion is enhanced with higher angles.

From the results of this study, we expect to elucidate the various glass surface deformations that occur owing to varied-angled UAV LiDAR flights and to assist in decision-making for UAV LiDAR flight planning, thereby expanding the potential applications of UAV LiDAR. Although applied research using UAV LiDAR is actively underway, data validation research focused on improving data accuracy is still lacking. In addition to glass surfaces, other land cover types with high transmittance and reflectance, such as solar panels, pipelines, mirrors, and water bodies, also pose challenges for LiDAR data collection. Therefore, further research is necessary to analyze and address the issue of data collection accuracy for these objects to maximize the usability of UAV LiDAR. Moreover, the deformations identified in this study as unique to glass surfaces in LiDAR point clouds, which are not observed in other objects, can be leveraged in a variety of future research endeavors. The geometric deformations of glass surfaces, such as point loss and distortion, identified in this study as unique 3D spatial characteristics of glass surfaces, can serve as a foundation for coordinate-based deep learning object detection and classification. These findings may also provide a basis for future research on restoring glass surface deformations. Furthermore, the observed intensity reduction on glass surfaces, which was the most distinct feature distinguishing glass surfaces from other objects, holds significant potential for window detection. By leveraging intensity and 3D coordinates as part of a four-channel object detection and classification framework, these studies hold promise to enhance the accuracy of point cloud classification and detection.

Acknowledgments

This work was partly supported by the Korea Institute of Energy Technology Evaluation and Planning (KETEP) grant funded by the Korea government (MOTIE) (20224000000290, Global Training Program of Human Resource for Smart Energy System) and the National Research Foundation of Korea (NRF) grant funded by the Korea government (MSIT) (NRF-2021R1A5A8033165).

References

1 S. R. Rogers, I. Manning, and W. Livingstone: Remote Sens. **12** (2020) 2806. https://doi.org/10.3390/rs12172806
2 H. N. Burns, C. G. Christodoulou, and G. D. Boreman: Opt. Eng. **30** (1991) 3. https://doi.org/10.1117/12.55801
3 J. Wojtanowski, M. Zygmunt, M. Kaszczuk, Z. Mierczyk, and M. Muzal: Opto-Electron. Rev. **22** (2014) 3. https://doi.org/10.2478/s11772-014-0190-2
4 K. Lim, P. Treitz, M. Wulder, B. St-Onge, and M. Flood: Prog. Phys. Geogr.: Earth Environ. **27** (2023) 1. https://doi.org/10.1191/0309133303pp360ra
5 X. Li, C. Liu, Z. Wang, X. Xie, D. Li, and L. Xu: Meas. Sci. Technol. **32** (2021) 3. https://doi.org/10.1088/1361-6501/abc867
6 A. Fidera, M. A. Chapman, and J. Hong: XXth ISPRS Congress **5** (2004) 880. https://www.researchgate.net/publication/228742357

7 J. S. Yun and J. Y. Sim: Proc. IEEE Conf. Computer Vision and Pattern Recognition (IEEE, Salt Lake City, 2018) 4597–4605. https://doi.org/10.1109/cvpr.2018.00483
8 X. Zhao, Z. Yang, and S. Schwertfeger: 2020 IEEE Int. Symp. Safety, Security, and Rescue Robotics (IEEE, 2020) 27–33. https://doi.org/10.1109/SSRR50563.2020.9292595
9 R. Koch, S. May, P. Murmann, and A. Nüchter: Rob. Auton. Syst. **87** (2017) 296. https://doi.org/10.1016/j.robot.2016.10.014
10 S. Soudarissanane, R. Lindenbergh, M. Menenti, and P. Teunissen: ISPRS J. Photogramm. Remote Sens. **66** (2011) 4. https://doi.org/10.1016/j.isprsjprs.2011.01.005
11 J. Sun, Z. Shen, Y. Wang, H. Bao, and X. Zhou: Proc. IEEE Conf. Computer Vision and Pattern Recognition (IEEE, Virtual, 2021) 8922–8931. https://doi.org/10.1109/cvpr46437.2021.00881
12 H. Mei, X. Yang, Y. Wang, Y. Liu, S. He, Q. Zhang, X. Wei, and R. W. H. Lau: Proc. IEEE Conf. Computer Vision and Pattern Recognition (IEEE, Virtual, 2020) 3687–3696. https://doi.org/10.1109/CVPR42600.2020.00374
13 Z. Li, Y. Yeh, and M. Chandraker: Proc. IEEE Conf. Computer Vision and Pattern Recognition (IEEE, Virtual, 2020) 1262–1271. https://doi.org/10.1109/cvpr42600.2020.00134
14 Z. Mao, X. Huang, H. Xiang, Y. Gong, F. Zhang, and J. Tang: Int. J. Appl. Earth Obs. Geoinf. **118** (2023) 103242. https://doi.org/10.1016/j.jag.2023.103242
15 Y. Gu, Y. Wang, T. Guo, C. Guo, X. Wang, C. Jiang, T. Cheng, Y. Zhu, W. Cao, Q. Chen, and X. Yao: Comput. Electron. Agric. **220** (2024) 108858. https://doi.org/10.1016/j.compag.2024.108858
16 G. Zheng, L. Ma, J. U. H. Eitel, W. He, T. S. Magney, L. M. Moskal, and M. Li: IEEE Trans. Geosci. Remote Sens. **55** (2016) 1. https://doi.org/10.1109/TGRS.2016.2611651
17 H. Fazeli, F. Samadzadegan, and F. Dadrasjavan: ISPRS Ann. Photogramm. Remote Sens. Spatial Inf. Sci. **41** (2016) 221. https://doi.org/10.5194/isprsarchives-xli-b6-221-2016
18 DJI Enterprise: https://enterprise.dji.com (accessed April 2023).
19 B. Alsadik and F. Remondino: ISPRS Int. J. Geo-Inf. **9** (2020) 6. https://doi.org/10.3390/ijgi9060378
20 R. Wang, J. Bach, and F. P. Ferrie: IEEE Workshop on Applications of Computer Vision (IEEE, 2011) 58–65. https://doi.org/10.1109/WACV.2011.5711484

About the Authors

Dohoon Kim received his B.S. and M.S. degrees from Kyungpook National University, South Korea, in 2022 and 2024, respectively. His research interests are in remote sensing, UAV, and LiDAR. (boxer80808006@gmail.com)

Kirim Lee received his B.S., M.S., and Ph.D. degrees from Kyungpook National University, South Korea, in 2016, 2018, and 2023, respectively. Since 2023, he has been a lecturer at Kyungpook National University. His research interests are in UAV, photogrammetry, and image processing. (geolee@knu.ac.kr)

Kourosh Khoshelham received his Ph.D. degree from Hong Kong Polytechnic University, China, in 2004. He was an assistant professor at Delft University of Technology and University of Twente before joining the University of Melbourne in 2015. Since 2015, he has been an associate professor at the University of Melbourne, Australia. His research interests are in photogrammetry, 3D computer vision, positioning, and navigation.
(k.khoshelham@unimelb.edu.au)

Hyeongil Shin received his B.S. and M.S. degrees from Kyungpook National University, South Korea, in 2022 and 2024, respectively. Currently, he is working on his Ph.D. degree at Kyungpook National University, South Korea. His research interests are in remote sensing, UAV, and image processing. (gusrlf6695@knu.ac.kr)

Won Hee Lee received his B.S. degree from Yonsei University, South Korea, in 2000, his M.S. degree from Seoul National University, South Korea, in 2003, and his Ph.D. degree from Ohio State University, United States, in 2008. From 2010 to 2015, he was an assistant professor at Chosun University, South Korea. Since 2015, he has been a professor at Kyungpook National University, South Korea. His research interests are in photogrammetry, GNSS, and remote sensing. (wlee33@knu.ac.kr)